Electronic structure and impurity-limited electron mobility of silicon superlattices

Srinivasan Krishnamurthy*
Department of Physics, University of Cincinnati, Cincinnati, Ohio 45219-0011

John A. Moriarty
Lawrence Livermore National Laboratory, University of California, Livermore, California 94550
(Received 4 March 1985)

With the utilization of a new complex-band-structure technique, the electronic structure of [100]-oriented model Si-$Si_{1-x}Ge_x$ and metal-oxide-silicon superlattices have been obtained over a wide range of layer thickness l ($11 \leq l \leq 110$ Å), complementing previous results obtained for very thin layer systems ($l \leq 11$ Å). For $l \geq 44$ Å, it is found that these systems exhibit a direct fundamental band gap, produced in large part by the Brillouin-zone folding of the bulk conduction-band edges. In the same range, the transverse band-edge electron effective mass is reduced to a limiting value of 0.73 of the bulk conductivity effective mass, supporting our previous suggestion that a band-structure-driven enhancement in transverse electron mobility over bulk silicon may be possible. Simple effective-mass scaling yields an enhancement of about 1.2 in the (low-temperature) impurity-scattering limit and about 2.2 in the (high-temperature) phonon-scattering limit. Detailed consideration is made of the simpler of the two cases, impurity-scattering-limited electron mobility, with the result that enhanced mobility is indeed predicted for sufficiently high carrier concentrations.

I. INTRODUCTION

The applications potential of artificial semiconductor superlattices has stimulated a corresponding interest in the basic physics of these systems. In contrast to the mainstream of fundamental research on systems derived from compound III-V and II-VI materials, our interest in semiconductor superlattices has focused on the nature and properties of structures created from elemental group-IV materials such as silicon. Within the confines of silicon materials technology (i.e., excluding III-V and II-VI materials) the number of feasible superlattice structures is, of course, greatly limited. With regard to conventional layered structures, the Si-$Si_{1-x}Ge_x$ system is perhaps the prototype silicon superlattice. In addition to our theoretical work on this system,[1] an increasing experimental interest in fabricating and studying Si-$Si_{1-x}Ge_x$ superlattices has also emerged.[2-5] Historically, the major experimental drawback to this type of structure has been the relatively large ($\approx 5\%$) lattice-constant mismatch between Si and Ge. It now appears, however, that this difficulty can be largely overcome[3-5] through the use of suitable strain-layer epitaxy.[6]

Beyond the Si-$Si_{1-x}Ge_x$ system, silicon materials technology also offers some other novel possibilities for superlattice structures. One is a metal-oxide-silicon (MOS) configuration with a grided metal electrode made up of fine parallel metal lines uniformly spaced on the oxide layer,[7] as illustrated in Fig. 1. In this system, it is envisioned that an extra periodic electron potential could be extended into the silicon by holding alternate metal lines in the grid at different voltages. The primary experimental challenge of creating such a system comes in producing a periodic metal electrode pattern of the ultrathin dimensions required (<500 Å line spacings and thicknesses). Fine-line technology is rapidly advancing to the point where this may be feasible.[8] A third possible silicon superlattice structure could be one consisting of alternately n- and p-doped silicon layers, as in the so-called n-i-p-i superlattice,[9] which in its own right has been actively investigated for III-V-compound-based superlattices.[10]

In a previous paper,[1] we formulated a realistic, but simplified, tight-binding (TB) model of the electronic structure of silicon superlattices that could be applied to all of the above cases. Straightforward application of the TB method, however, was limited to systems with layer thickness $l \leq 11$ Å, because the size of the Hamiltonian matrix increases linearly with l. We have now combined this model with a new complex-band-structure technique, generalized from a method developed by Schulman and Chang for III-V compound systems,[11] in which the size of the Hamiltonian matrix does not increase with layer thickness. We report here both the details of our method as well as comprehensive electronic structure results ob-

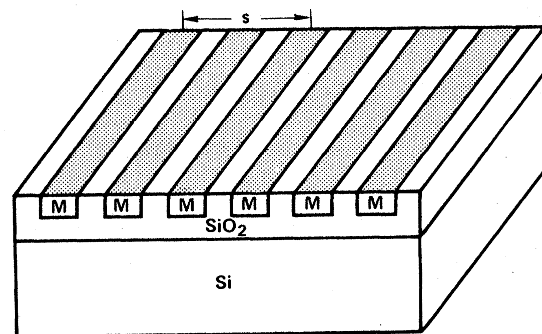

FIG. 1. Conceptual drawing of a possible MOS superlattice structure.

 ©1985 The American Physical Society

tained for silicon superlattices over the complementary range $11 \leq l \leq 110$ Å, using this new technique.

One very interesting question with regard to silicon superlattices is whether or not a band-structure-driven enhancement in electron mobility, related to the special nature of silicon's bulk band gap, is possible. The initial experiments on Si-$Si_{1-x}Ge_x$ systems[2] showed, in fact, systematically enhanced transverse electron mobility in [100]-oriented samples, even at room temperature and without deliberate modulation doping. Samples oriented in a [111] direction, on the other hand, did not display such an enhancement. Consistent with this observation, we pointed out in Ref. 1 that [100]-oriented silicon superlattices could have a reduced band-edge transverse conductivity effective mass, while [111]-oriented superlattices would not. Moreover, the expected magnitude of effective-mass reduction appears to be in line with the degree of observed enhancement. It remains uncertain, however, whether or not this effect is actually playing the decisive role in raising the mobility. For one thing, the experimental results were obtained on relatively thick-layer (> 300 Å) systems, where such a quantum effect could be greatly diminished. Secondly, the Si-$Si_{1-x}Ge_x$ superlattices employed in this study were not grown by strain-layer epitaxy, so that the quality of the interfaces was not well controlled. Possible interface effects and other nonuniformities cloud any simple interpretation of the experimental results in terms of our theoretical model. Nonetheless, the nature of electron mobility in these systems has clearly become a matter for more careful investigation. As a theoretical step in this direction, we have applied our present electronic structure results to the first full calculations of impurity-scattering-limited electron mobility in silicon superlattices.

In Sec. II we first review our basic model for the electronic structure of silicon superlattices, then discuss our complex-band-structure method for dealing with arbitrarily thick layers, and finally present our calculated results. In Sec. III we address the problem of electron mobility in these systems and elaborate on our results for both drift and Hall mobility in the impurity-scattering limit. We conclude in Sec. IV.

II. SUPERLATTICE BAND STRUCTURE

A. General theoretical model

We consider a [100]-oriented silicon superlattice of alternating A and B layers with an underlying tetrahedral symmetry of the bulk diamond lattice, as illustrated in Fig. 2. We envisage that layer A consists of pure Si atoms, while layer B either contains a second species (Ge in $Si_{1-x}Ge_x$) or represents Si atoms where the electron potential has been rigidly raised or lowered by some amount (as in an MOS or n-i-p-i superlattice). As in Ref. 1, we assume equal A- and B-layer thicknesses and a common bulk bond length d, so that the superlattice repeats in the x direction with a period

$$s = 2l = n_s a/2 , \tag{1}$$

where $a = 4d/\sqrt{3}$ is the lattice constant of pure silicon

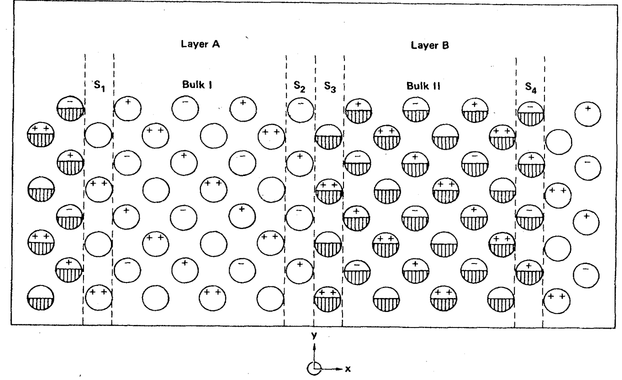

FIG. 2. Schematic diagram of the $n_s = 8$ superlattice geometry, showing the projection of four planes of atoms onto the $z = 0$ plane. The unhatched circles represent the Si atoms of layer A, while the hatched circles represent the atoms of layer B. Atoms belonging to the planes $z = -a/4$, $a/4$, and $a/2$ are marked $-$, $+$, and $++$, respectively. The bulk regions I and II and interface layers S_1, S_2, S_3, and S_4 apply to the complex-band-structure technique discussed in the text.

and n_s is an integer. In the case of Si-$Si_{1-x}Ge_x$ we are thus neglecting the slight increase in bond length in the alloy layer. We also deal here with the case of even n_s, so that the superlattice always possesses simple tetragonal symmetry.

In a minimal-basis TB description of the electronic structure, consisting of one s and three p atomic orbitals per site, the interatomic matrix elements coupling one atom to another are primarily a function of bond length,[12] varying approximately as d^{-2}. Since d is fixed in our model, these quantities remain the same in the superlattice as in bulk silicon, for which we have obtained carefully fitted nearest and second-nearest-neighbor values.[1] The silicon intra-atomic energies ε_s and ε_p of layer A, on the other hand, are modified in layer B to some values $\varepsilon_s + V_s^{(s)}$ and $\varepsilon_p + V_s^{(p)}$. The case

$$V_s = V_s^{(s)} = V_s^{(p)} \tag{2}$$

corresponds to a MOS or n-i-p-i superlattice in which the electron potential is rigidly raised by an amount V_s in layer B. We have designated this as type-I behavior. The opposite limiting case

$$V_s = -V_s^{(s)} = V_s^{(p)} , \tag{3}$$

in which s and p electrons effectively see equal and opposite average potentials, turns out to be an appropriate model, within the virtual-crystal approximation, for the alloy component in the Si-$Si_{1-x}Ge_x$ superlattice.[1] We have designated this as type-II behavior. In this case, we have further derived[1] an approximate empirical relationship between V_s and the Ge concentration x of the form

$$V_s \approx (0.5 \pm 0.1)x \text{ eV} . \tag{4}$$

In both the type-I and type-II models, therefore, we are left with two free parameters: n_s, representing layer

thickness, and V_s, representing the physical or chemical strength of the superlattice potential.

Band bending and other nonideal interface effects may be incorporated into our model by allowing, for example, V_s to grow smoothly across several layers at the interface instead of changing abruptly from zero. We have considered a number of such graded-layer calculations, but they produce results so qualitatively and quantitatively similar to the ideal case that we shall not consider this complication further in the present discussion.

B. Tight-binding complex-band-structure method (TB-CBM)

A primitive unit cell of the superlattice contains $2n_s$ atoms, so that with four orbitals per site the TB Hamiltonian matrix is $8n_s \times 8n_s$ in size. For $n_s = 8$ (corresponding to $l = 11$ Å), the matrix is already 64×64, and hence the calculation of the electronic structure in this manner becomes intractable for even modestly thick layers. The complex-band-structure technique of Schulman and Chang[11] nicely overcomes this difficulty. In this method, one views the superlattice as being composed of bulk regions in each layer separated by interface planes, as shown in Fig. 2. The number of atomic interface planes is taken such that the atoms in bulk regions I and II are not directly coupled: for second-neighbor interactions, two planes at each interface are required. One then capitalizes on the fact that the solutions to Schrödinger's equation are local and, hence, in the bulk regions must be some linear combination of bulk states including both extended Bloch states (real **k**) and evanescent states (complex **k**). For a given energy E, there are in our case a maximum of 16 possible **k** states in each bulk region.[13] These states, together with two-dimensional Bloch sums of atomic orbitals centered on the interface-plane atoms, can be used to expand the superlattice wave function in the form

$$\psi_{\mathbf{q}}(\mathbf{r},E) = \frac{1}{\sqrt{N_L}} \sum_{\mathbf{L}} e^{i\mathbf{q}\cdot\mathbf{L}} \left[\sum_{\sigma,i} A^{\sigma}_{\mathbf{k}_i}(\mathbf{q}) \psi^{\sigma}_{\mathbf{k}_i}(\mathbf{r}-\mathbf{L},E) + \sum_{n,\alpha} B^{n}_{\alpha}(\mathbf{q}) \phi^{n}_{k_{\parallel}\alpha}(\mathbf{r}-\mathbf{L}) \right], \tag{5}$$

where $\mathbf{q} = q_x\hat{\mathbf{x}} + \mathbf{k}_{\parallel}$ is the superlattice wave vector, $\mathbf{L} = ms\hat{\mathbf{x}}$, with m an integer, $\mathbf{k}_i = k_x^i\hat{\mathbf{x}} + \mathbf{k}_{\parallel}$ is a bulk wave vector ($i = 1,16$), $\psi^{\sigma}_{\mathbf{k}_i}$ is the corresponding bulk wave function for region σ (σ=I,II in Fig. 2), and $\phi^{n}_{\mathbf{k}_{\parallel}\alpha}$ is a two-dimensional Bloch state for interface plane S_n ($n = 1,2,3,4$ in Fig. 2) and atomic orbital α ($\alpha = s, p_x, p_y, p_z$). The wave vector $\mathbf{k}_{\parallel}$ is contained entirely within the transverse plane (here the y-z plane) and is common to both the bulk and the superlattice. The resulting Hamiltonian matrix is of size 48×48 independent of layer thickness.

The price that must be paid for a fixed Hamiltonian-matrix size is an energy-dependent basis, requiring an iteration procedure to calculate the superlattice band structure self-consistently. For given values of n_s and V_s one fixes the superlattice wave vector **q** and selects a trial energy $E = E_t$ to be used in Eq. (5). For the chosen E_t, the 16 bulk states for each region are obtained. This information is contained in the complex band structure of the bulk material,[14,15] which need only be generated once for each layer from the appropriate 8×8 bulk TB Hamiltonians. The [100] complex band structure of bulk silicon obtained from our TB parameters, and appropriate to layer A for all V_s and n_s, is shown in Fig. 3. In the type-I case, rigidly shifting this band structure upward by an amount V_s, corresponding to intra-atomic energies $\varepsilon_s + V_s$ and $\varepsilon_p + V_s$, makes it also appropriate to layer B. In the type-II case, however, the complex band structure for layer B must be recalculated with intra-atomic energies $\varepsilon_s - V_s$ and $\varepsilon_p + V_s$ for each V_s. The 48×48 superlattice Hamiltonian is then set up and diagonalized to obtain the true superlattice energy E_s for the assumed basis. One iterates this procedure until $E_s = E_t$ to some acceptable tolerance. In our procedure, an accuracy of 10^{-5} eV in energy is achieved with typically five iterations in less than 1 min of central-processing-unit (CPU) time. By varying **q**, the complete superlattice band structure may be mapped out in this way.

Our tight-binding complex-band-structure method (TB-CBM) improves upon that of Schulman and Chang[11] in several important ways. First, our TB model includes second-neighbor interactions as well as the first-neighbor interactions considered by them. Second, Schulman and Chang supplemented the bulk basis states $\psi^{\sigma}_{\mathbf{k}_i}$ with only

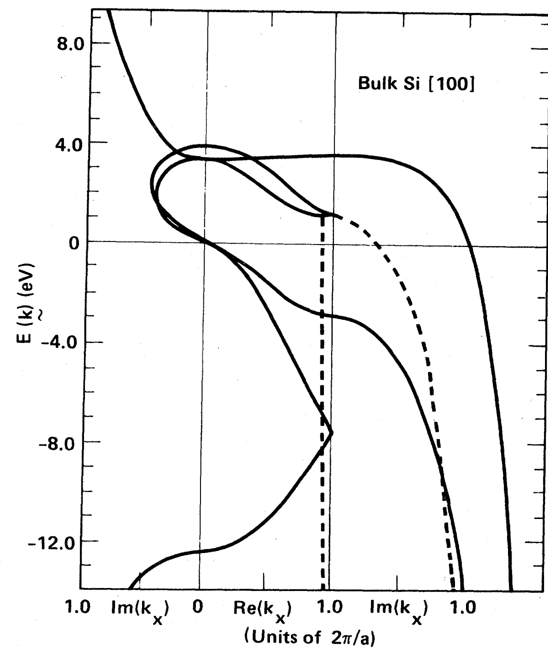

FIG. 3. Complex band structure of bulk silicon in the [100] direction with $\mathbf{k} = k_x\hat{\mathbf{x}}$. Left-hand panel, complex bands with $\mathrm{Re}(k_x) = 0$; center panel, real bands with $\mathrm{Im}(k_x) = 0$ (solid lines) and real part of the complex band associated with the conduction-band edge (dashed line); right-hand panel, complex bands with $\mathrm{Re}(k_x) = 2\pi/a$ (solid lines) and corresponding imaginary part of the complex band associated with the conduction-band edge (dashed line).

atomic orbitals α on the interface planes, restricting their approach to the longitudinal $\mathbf{k}_{\parallel}=0$ band structure. Utilizing instead Bloch orbitals of the form

$$\phi^{n}_{\mathbf{k}_{\parallel}\alpha}(\mathbf{r})=\frac{1}{\sqrt{N_{\parallel}}}\sum_{j}\alpha(\mathbf{r}-\tau_{jn})e^{\mathbf{k}_{\parallel}\cdot\tau_{jn}} , \quad (6)$$

where j spans the $N_{\parallel}$ atoms in the interface plane n, allows us to obtain the entire superlattice electronic structure and, in particular, the transverse $q_x=0$ energy bands. Finally, in constructing the superlattice Hamiltonian from the basis (5), we have included certain finite-layer corrections to the bulk regions that are necessary to make the method exact and which were neglected by Schulman and Chang. These corrections become vanishingly small as $n_s\rightarrow\infty$, but significantly affect fine details of the band structure such as effective masses for the range of n_s considered here.

The physical origin of the finite-layer corrections lies in the fact that the bulk regions I and II are not infinitely periodic in the x direction. That is, the $\psi^{\sigma}_{\mathbf{k}_i}$ are not truely exact eigenstates of the σ-region portion of the superlattice Hamiltonian H_{SL}, but rather one has

$$\langle\psi^{\sigma}_{\mathbf{k}_i}(\mathbf{r},E)\,|\,H_{\mathrm{SL}}\,|\,\psi^{\sigma}_{\mathbf{k}_j}(\mathbf{r},E)\rangle=E\delta_{ij}+\delta B(E,\mathbf{k}_i,\mathbf{k}_j) , \quad (7)$$

where the correction term δB is on the order of $1/n_s$. One can attempt to derive an expression for δB directly, but we have found it more convenient to simply evaluate the matrix elements on the left-hand side of Eq. (7) by writing the bulk states in the form

$$\psi^{\sigma}_{\mathbf{k}_i}(\mathbf{r},E)=\frac{1}{\sqrt{N_{\parallel}}}\sum_{\alpha,\mu}\frac{1}{[N_{\mu}(\mathbf{k}_i)]^{1/2}}C^{\sigma}_{\alpha\mu}(\mathbf{k}_i,E)\times\sum_{j,n}\alpha(\mathbf{r}-\tau^{\mu}_{jn})e^{i\mathbf{k}_i\cdot\tau^{\mu}_{jn}} , \quad (8)$$

where

$$N_{\mu}(\mathbf{k}_i)=\sum_{n}\exp[-i(\mathbf{k}^{*}_i-\mathbf{k}_i)\cdot\tau^{\mu}_{jn}] \quad (9)$$

is a normalization factor independent of j such that

$$\sum_{\alpha,\mu}|\,C^{\sigma}_{\alpha\mu}(\mathbf{k}_i,E)\,|^2=1 . \quad (10)$$

Here μ spans the two (anion and cation) sites of the bulk basis and n spans the n_s-2 planes of the bulk regions. Note that for real $\mathbf{k}_i$, $N_{\mu}=n_s-2$. The expansion coefficients $C^{\sigma}_{\alpha\mu}(\mathbf{k}_i,E)$ are established from the complex band structures of the bulk regions.

With the basis states $\phi^{n}_{\mathbf{k}_{\parallel}\alpha}$ and $\psi^{\sigma}_{\mathbf{k}_i}$ referred back to the atomic orbitals α through Eqs. (6) and (8), it is, in fact, straightforward to generate the entire 48×48 superlattice Hamiltonian matrix by applying the basic ground rules of our TB model for orbitals centered on sites $\mathbf{R}_i$ and $\mathbf{R}_j$, namely

$$\langle\alpha(\mathbf{r}-\mathbf{R}_i)\,|\,\alpha'(\mathbf{r}-\mathbf{R}_j)\rangle=\delta_{\alpha\alpha'}\delta_{ij} ; \quad (11)$$

for $i=j$,

$$\langle\alpha(\mathbf{r}-\mathbf{R}_i)\,|\,H_{\mathrm{SL}}\,|\,\alpha'(\mathbf{r}-\mathbf{R}_i)\rangle=\delta_{\alpha\alpha'}\times\begin{cases}\varepsilon_{\alpha} & (\text{layer } A),\\ \varepsilon_{\alpha}\pm V_s & (\text{layer} B),\end{cases} \quad (12)$$

and for $i\neq j$,

$$\langle\alpha(\mathbf{r}-\mathbf{R}_i)\,|\,H_{\mathrm{SL}}\,|\,\alpha'(\mathbf{r}-\mathbf{R}_j)\rangle=\begin{cases}V^{(1)}_{\alpha\alpha'} & (\text{first neighbors}),\\ V^{(2)}_{\alpha\alpha'} & (\text{second neighbors}),\\ 0 & (\text{otherwise}) .\end{cases} \quad (13)$$

The resulting matrix is too lengthly to reproduce here, but will be provided to the interest reader upon request. The TB quantities ε_{α}, $V^{(1)}_{\alpha\alpha'}$, and $V^{(2)}_{\alpha\alpha'}$ as used in our calculations are tabulated in Ref. 1.

It should be noted that Eq. (7) implies that the bulk states $\psi^{\sigma}_{\mathbf{k}_i}$ are not orthogonal to one another for different $\mathbf{k}_i$ in the same region σ. Before attempting to diagonalize the superlattice Hamiltonian matrix, it is convenient to first make a unitary transformation to an orthonormal basis. We do this, in practice, numerically by a standard Gram-Schmidt procedure.

Finally, we have tested the exactness of out TB-CBM scheme in three separate ways: (i) for $V_s=0$, the bulk silicon energy levels are reproduced; (ii) for $n_s=8$ and any V_s, the TB-CBM results obtained here are identical to the TB results of Ref. 1; and (iii) removing outer planes from the bulk layers and treating them as additional interface planes has no effect on the calculated energy bands. Removing the interface layers, on the other hand, does alter the results, as expected.

C. Electronic structure results

TB-CBM calculations of the silicon superlattice band structure have now been carried out for $8\leq n_s\leq 80$ ($11\leq l\leq 110$ Å) and $0\leq V_s\leq 1.0$ eV for both the type-I and type-II cases. In particular, the magnitude of the fundamental band gap, conduction-band-edge positions, and band-edge effective masses have been obtained over these parameter ranges. The variation of the band-gap magnitude E_g with V_s for selected values of n_s is shown in Figs. 4 and 5 for the type-I and type-II superlattices, respectively. In both cases, E_g decreases with increasing V_s and n_s, but the E_g-versus-V_s curve quickly saturates for large n_s. Extrapolation of the $n_s=80$ curves in Figs. 4 and 5 suggests that the band gap will close for $V_s=1.11$ eV, the bulk silicon band gap, in the limit $n_s\rightarrow\infty$, as rigorously required in the type-I case.

While the valence-band edge remains stationary at the $\mathbf{k}=0$ Brillouin-zone center (Γ point), the positions of the conduction-band edges change as V_s or n_s is increased. In general, the effective sixfold degeneracy of the bulk band edges is lifted in the superlattice, with the [100] and [$\bar{1}$00] edges folded back towards Γ and lowered in energy relative to the remaining [010], [0$\bar{1}$0], [001], and [00$\bar{1}$] edges, which remain close to the Brillouin-zone-boundaries (X points). For $n_s\geq 32$ ($l\geq 44$ Å) the former two edges become degenerate at Γ and a direct band gap results. This situation is illustrated in Fig. 6, where the complete longitudinal [100] and transverse [001] band structure $E(\mathbf{q})$ in the vicinity of the fundamental gap is plotted in a typical case. The energy difference Δ between the X and Γ

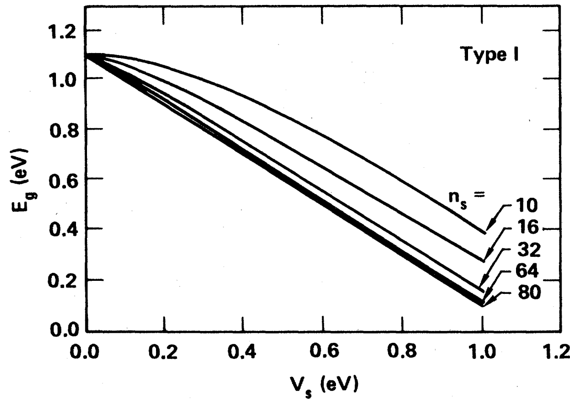

FIG. 4. Variation of the fundamental energy-band gap E_g with V_s for the type-I superlattice at five layer thicknesses.

conduction-band edges always remains small (≤ 0.0065 eV $=75$ K), however, and eventually declines back to zero as $n_s \rightarrow \infty$, as shown in Fig. 7.

The pronounced flattening of the [100] superlattice bands, seen in Fig. 6, leads to very large (essentially infinite) longitudinal effective masses. The transverse effective masses, on the other hand, display much weaker dependencies on V_s and n_s, with values both above and below the bulk possible. Figure 8 illustrates the behavior of the valence-band-edge transverse hole mass α_t relative to the (calculated) heavy-hole mass of the bulk for the type-I and type-II superlattices. In the type-I case, α_t saturates near 1.0 for large n_s, while in the type-II case, α_t displays a small linear decrease with increasing V_s even for large n_s. The corresponding conduction-band-edge transverse electron mass β_t relative to the bulk transverse electron mass is shown in Fig. 9 for the type-II superlattice. The type-I results are almost identical, and in both cases β_t saturates at 1.0 for $n_s \geq 32$.

III. ELECTRON MOBILITY

The possibility of enhanced carrier mobilities in semiconductor superlattices is a subject of fundamental as well

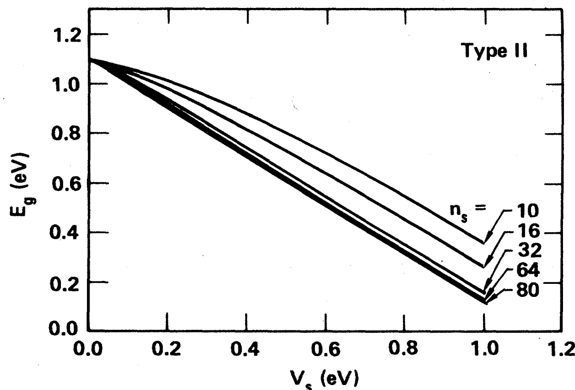

FIG. 5. Variation of the fundamental energy-band gap E_g with V_s for the type-II superlattice at five layer thicknesses.

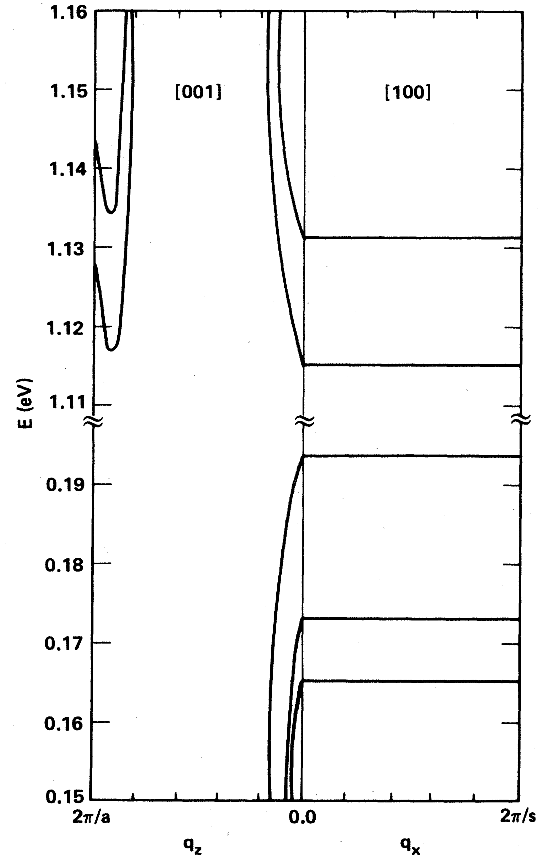

FIG. 6. Longitudinal [100] and transverse [001] band structures near the fundamental band gap of a type-II superlattice with $n_s = 64$ and $V_s = 0.2$ eV. The bands shown are those thermally accessible to mobile charge carriers at room temperature.

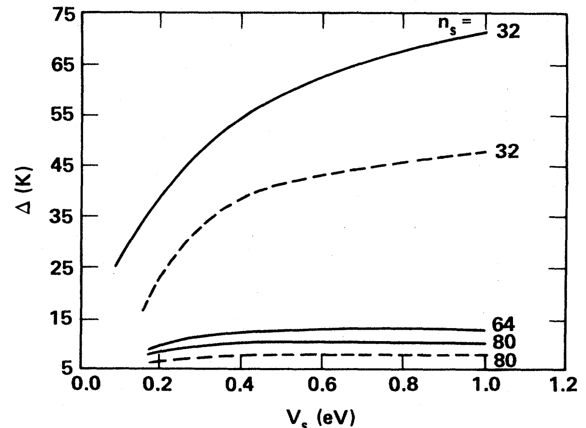

FIG. 7. Energy difference Δ between the X- and Γ-point conduction-band minima vs V_s for various type-I and type-II superlattices. (Solid lines, type-I; dashed lines, type-II.) The $n_s = 64$, type-II result has been omitted for clarity.

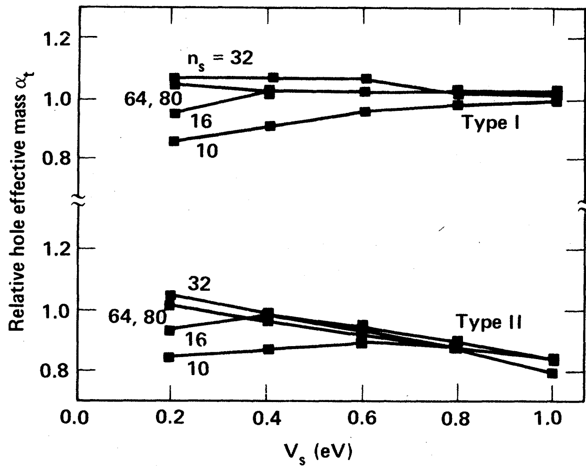

FIG. 8. Relative band-edge transverse hole effective mass α_t vs V_s for various n_s in the type-I and type-II superlattices.

as applied interest. It is well known that for III-V superlattices, such as GaAs-$Ga_{1-x}Al_xAs$, the preparation technique of modulation doping can reduce impurity scattering and raise carrier mobility dramatically at low temperatures.[16,17] Previously,[1] we suggested that a quite different enhancement mechanism, one driven by reduced transverse conductivity effective masses associated with the superlattice band structure, also appeared to be possible in silicon superlattices. We have now addressed this question more fully, and in the case of impurity scattering we have done actual transport calculations, based on the above band-structure results, to obtain realistic upper limits on electron mobility enhancement at low temperature in uniformly doped silicon superlattices

In the superlattice, the usual isotropic conductivity effective mass for electrons in bulk silicon,

$$m_c^* = \frac{3}{[(1/m_l^*)+(2/m_t^*)]} , \tag{14}$$

is replaced by separate values perpendicular (i.e., longitudinal) and parallel (i.e., transverse) to the layers. For a single conduction band at Γ, for example, one can write, for these latter quantities,

$$m_{eL}^* = \beta_l m_l^* \tag{15}$$

and

$$m_{eT}^* = \beta_t m_t^* , \tag{16}$$

respectively, where β_l and β_t are the enhancement factors of the bulk longitudinal and transverse band masses m_l^* and m_t^*. As discussed above, $\beta_l \gg 1$ due to the band flattening in the longitudinal direction, while $\beta_t \approx 1$. Because of the more favorable averaging of the relatively small transverse band mass m_t^* in the superlattice than the bulk, however, the effective transverse conductivity mass is reduced by a factor

$$\gamma_T \equiv m_{eT}^* / m_c^* = 0.73\beta_t , \tag{17}$$

where in the last equality m_t^*/m_c^* has been evaluated from the known values of $m_l^* = 0.97m$ and $m_t^* = 0.19m$ for bulk silicon.[18] Ideally, for ionized-impurity scattering the mobility should be enhanced by a factor of $\gamma_T^{-1/2}$ and for acoustic-phonon scattering by a factor of $\gamma_T^{-5/2}$, if these are the only energy bands involved in the transport. These factors are plotted in Fig. 10 as a function of V_s for selected n_s in the type-II superlattice. Because $\beta_t \rightarrow 1$ rapidly as n_s increases, one approaches the saturation values of $\gamma_T^{-1/2} = 1.17$ and $\gamma_T^{-5/2} = 2.20$ for even modestly thick layers.

Of course, additional considerations enter the picture beyond band-edge effective masses. For example, the bulk conduction-band edges which split away and above in energy in the superlattice will always be accessible at a high enough temperature. In practice, a thermal average of the scattering over a number of bands is necessary to establish the effective carrier mobility. Moreover, a different

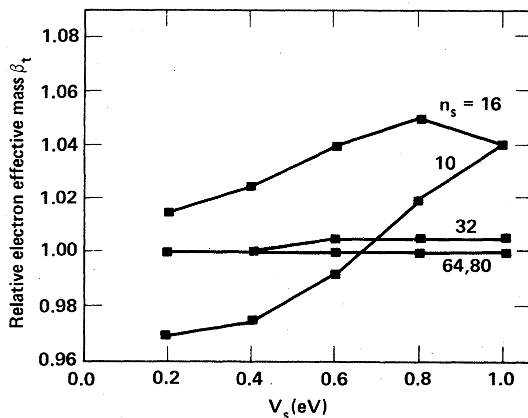

FIG. 9. Relative band-edge transverse electron effective mass β_t vs V_s for various n_s in the type-II superlattice.

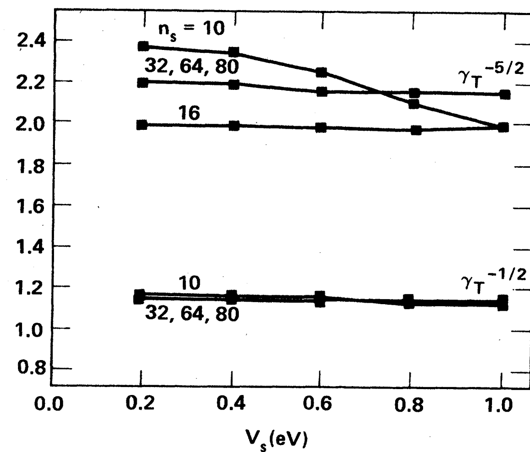

FIG. 10. Impurity-scattering-limited and phonon-scattering-limited enhancement factors $\gamma_T^{-1/2}$ and $\gamma_T^{-5/2}$ vs V_s for various n_s in the type-II superlattice. The $n_s = 16$ result for $\gamma_T^{-1/2}$ has been omited for clarity.

thermal average, which weights the low-energy states more heavily in the superlattice than in the bulk, is usually appropriate. In the bulk, the conduction-band-edge constant-energy surfaces are ellipsoidal in shape and the density of states for a single band has the familiar form

$$N_c(E)=\frac{1}{\hbar^3\pi^2}m_t^*(2m_l^*)^{1/2}(E-E_c)^{1/2}\ , \tag{18}$$

where E_c is the conduction-band edge. In the superlattice, on the other hand, the band flattening mentioned above makes the constant-energy surfaces more nearly cylindrical in shape, so that the corresponding density of states is proportional to that of a two-dimensional electron gas. For a single conduction band at Γ,

$$N_c(E)=\frac{1}{\hbar^2\pi s}\beta_t m_t^*\ , \tag{19}$$

which is independent of energy.

In our present studies, we have considered ionized-impurity scattering of electrons from the screened Coulomb potential

$$v_I(r)=-\frac{e^2}{\kappa}\frac{e^{-\lambda r}}{r}\ , \tag{20}$$

where κ is the dielectric constant of the host and λ^{-1} is the Debye length, $\lambda^2=4\pi n_I e^2/(\kappa k_B T)$, for uniform doping to a concentration n_I. The scattering time $\tau(E)$ for scattering from state $\mathbf{k}$ to state $\mathbf{k}'$ on the constant-energy surface $E(\mathbf{k})$ is calculated from the familiar transport formula

$$\frac{1}{\tau(E)}=\frac{\Omega^2 n_I}{(2\pi\hbar)^2}\times\int(1-\cos\theta)\,|\langle\psi_{\mathbf{k}}|v_I|\psi_{\mathbf{k}'}\rangle|^2\frac{\hbar}{|\nabla E(\mathbf{k})|}dS_E\ , \tag{21}$$

where Ω is the volume of the solid and the integral is over the constant-energy surface. In bulk silicon, where the density of states (18) is operative for each conduction-band edge, the corresponding mobility of nondegenerate electrons, $\mu_B=e\langle\tau(E)\rangle/m_c^*$, is well approximated by the standard form[19]

$$\mu_B=\frac{32\kappa^2}{(8\pi^3)^{1/2}e^3}\frac{(k_BT)^{3/2}}{n_I(m_c^*)^{1/2}}G_B(n_I,T,m_c^*)\ , \tag{22}$$

where G_B is a slowly varying function of n_I, T, and m_c^* given by

$$G_B(n_I,T,m_c^*)=\int_0^\infty \varepsilon e^{-\varepsilon}F_B^{-1}(\varepsilon)d\varepsilon\ , \tag{23}$$

with $\varepsilon=(E-E_c)/k_BT$,

$$F_B(\varepsilon)=\tfrac{3}{2}\int_0^\pi\frac{A_B(\varepsilon,\theta)\sin\theta(1-\cos\theta)}{[\varepsilon\sin^2(\theta/2)+\varepsilon_B]}d\theta\ , \tag{24}$$

and $\varepsilon_B=\lambda^2\hbar^2/(8m_c^*k_BT)$. In Eq. (24) the term $A_B(\varepsilon,\theta)$ reflects the wave-function dependence of the scattering, that is, the departure of $\psi_{\mathbf{k}}$ from a plane wave. In practice, this quantity turns out to be remarkably close to unity for all ε and θ of interest, so that we simply average it over energy and scattering angle and remove it from the integrals as a factor ≈ 1.

In the superlattice, a parallel calculation, but with the scattering taking place on a cylindrical energy surface corresponding to a constant density of states like (19), yields, for the ith conduction band,

$$\mu_{\mathrm{SL}}^i=\frac{15s\kappa^{3/2}}{4\pi\sqrt{2}e^2}\frac{k_BT}{(n_I m_{e\mathrm{T}}^*)^{1/2}}G_{\mathrm{SL}}(n_I,T,m_{e\mathrm{T}}^*)\ , \tag{25}$$

neglecting interband scattering. Here G_{SL} is also a slowly varying function of the same form as Eq. (23) with F_B replaced by F_{SL} given by

$$F_{\mathrm{SL}}(\varepsilon)=\frac{15}{8}\left[\frac{\varepsilon_{\mathrm{SL}}}{\pi}\right]^{1/2}\int_0^\pi\frac{A_{\mathrm{SL}}(\varepsilon,\theta)(1-\cos\theta)}{[\varepsilon\sin^2(\theta/2)+\varepsilon_{\mathrm{SL}}]^2}d\theta\ , \tag{26}$$

with $\varepsilon_{\mathrm{SL}}=\lambda^2\hbar^2/(8m_{e\mathrm{T}}^*k_BT)$. The wave-function-dependent quantity $A_{\mathrm{SL}}(\varepsilon,\theta)$ behaves very much like $A_B(\varepsilon,\theta)$ and we treat it in an analogous manner.

In Eqs. (25) and (26), $m_{e\mathrm{T}}^*$ is the appropriate transverse conductivity mass for the ith band. For band minima at Γ, this is given by Eq. (16). For band minima near the X points along the [010], [0$\bar{1}$0], [001], and [00$\bar{1}$] directions, on the other hand, a weighted average

$$m_{e\mathrm{T}}^*=\frac{2}{[1/(\beta_l m_l^*)+1/(\beta_t m_t^*)]} \tag{27}$$

is appropriate. In the latter case, longitudinal l and transverse t are defined in the y-z plane with respect to the axis of symmetry, so that both β_l and β_t in Eq. (27) are on the order of unity. Note that with $m_l^*>m_t^*$ the constant-energy surfaces for the X-point minima are elliptical cylinders.

In the superlattice mobility μ_{SL}^i, the inverse-square-root effective-mass dependence of the bulk is recovered, as expected, but the temperature and impurity concentration dependencies now reflect the two-dimensional nature of the transport. Summing contributions from all thermally accessible conduction bands i, the average electron drift mobility in the superlattice is given by

$$\mu_{\mathrm{SL}}=\sum_i n_i\mu_{\mathrm{SL}}^i/n_I\ , \tag{28}$$

where n_i is the electron concentration in the ith band. For $T\le 300$ K, the conduction bands which must be included in Eq. (28) are shown in Fig. 6.

For a typical silicon superlattice, the calculated relative mobility μ_{SL}/μ_B based on Eqs. (20)—(28) is plotted in Fig. 11 as a function of n_I for selected values of T, and in Fig. 12 as a function of T for selected values of n_I. It can be seen that, at low temperatures, where impurity scattering dominates other scattering mechanisms, an enhancement in electron mobility is indeed possible for sufficiently high carrier concentrations. The qualitative variations found with n_I and T are most easily understood by considering the high-temperature limit of Eqs. (22) and (25). In this limit, $G_B=[\ln(3/\varepsilon_B)]^{-1}$ and $G_{\mathrm{SL}}=1$, so that

$$\frac{\mu_{\mathrm{SL}}}{\mu_B}=C_1\left[\frac{n_I}{T}\right]^{1/2}\ln\left[\frac{C_2T^2}{n_I}\right]\ , \tag{29}$$

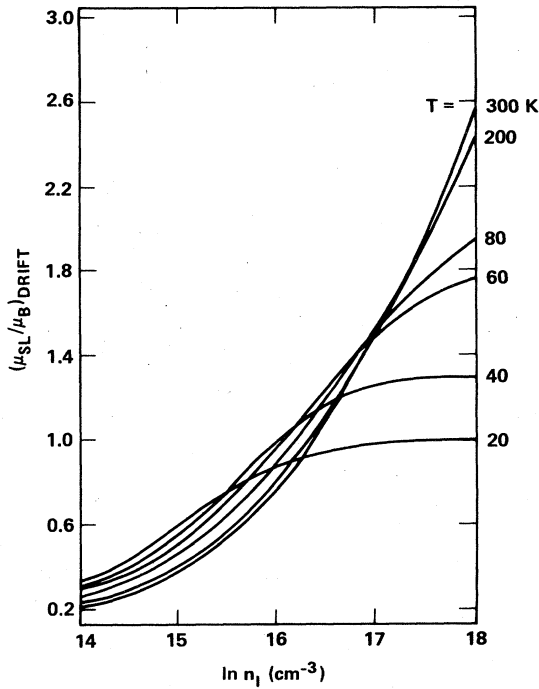

FIG. 11. Variation of the impurity-scattering-limited electron drift mobility with donor concentration n_I at selected temperatures for a type-II superlattice, where $n_s = 64$ and $V_s = 0.2$ eV, relative to bulk silicon.

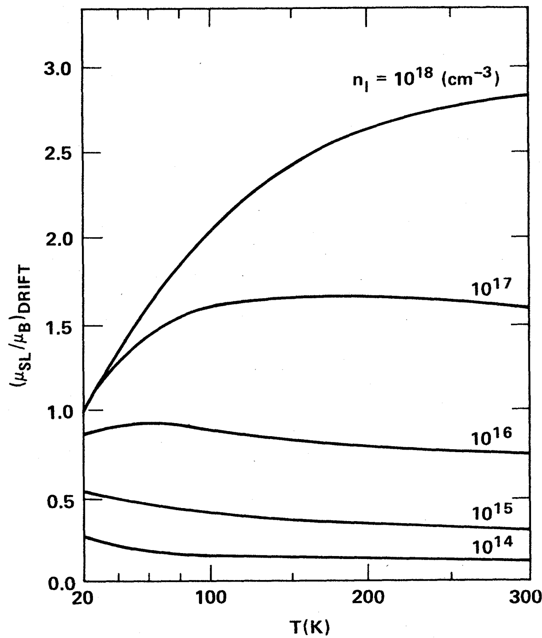

FIG. 12. Variation of the impurity-scattering-limited electron drift mobility with temperature T for selected donor concentrations, as in Fig. 11.

where C_1 and C_2 are constants. For a fixed T in the range of interest, this function increases to a maximum for some n_I and then decreases monotonically. Similarly, for a fixed n_I, this function increases to a maximum for some T and then decreases.

The corresponding Hall mobility in the superlattice may be calculated by replacing Eq. (28) by the average

$$\sum_i r_i n_i (\mu_{\rm SL}^i)^2 \Big/ \sum_i n_i \mu_{\rm SL}^i \; , \qquad (30)$$

where r_i is a weighting factor reflecting the energy dependence and anisotropy of the scattering and is given by

$$r_i = \frac{\langle \tau_i^2(E) \rangle}{\langle \tau_i(E) \rangle^2} C \; , \qquad (31)$$

where for Γ-point minima $C = 1$, while for X-point minima

$$C = \frac{4K}{(K+1)^2} \; , \qquad (32)$$

with

$$K = \beta_l m_l^* / (\beta_t m_t^*) = 5.1 \beta_l / \beta_t$$

and β_l and β_t are defined as in Eq. (27). In contrast, for bulk silicon,

$$C = \frac{3K(K+2)}{(2K+1)^2} = 0.87 \; , \qquad (33)$$

with $K = m_l^* / m_t^* = 5.1$. Our calculated relative Hall mobility is plotted in Fig. 13 as a function of n_I for selected values of T, and in Fig. 14 as a function of T for selected values of n_I, both for the same superlattice parameters as in Figs. 11 and 12. Similar trends but somewhat lower magnitudes are clearly seen.

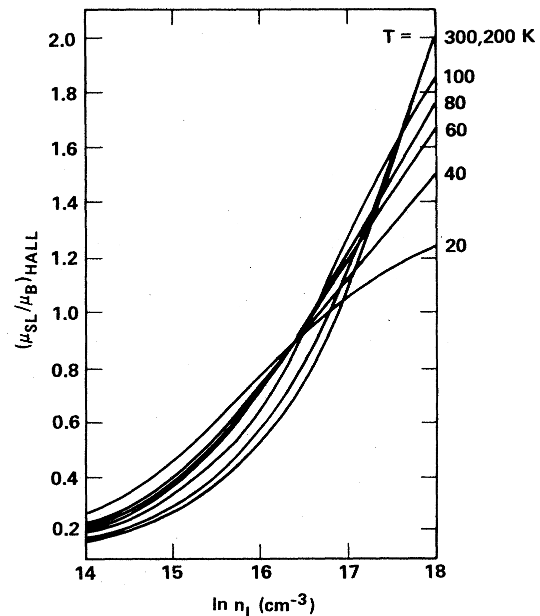

FIG. 13. Variation of the impurity-scattering-limited electron Hall mobility with donor concentration n_I at selected temperatures for a type-II superlattice, where $n_s = 64$ and $V_s = 0.2$ eV, relative to bulk silicon.

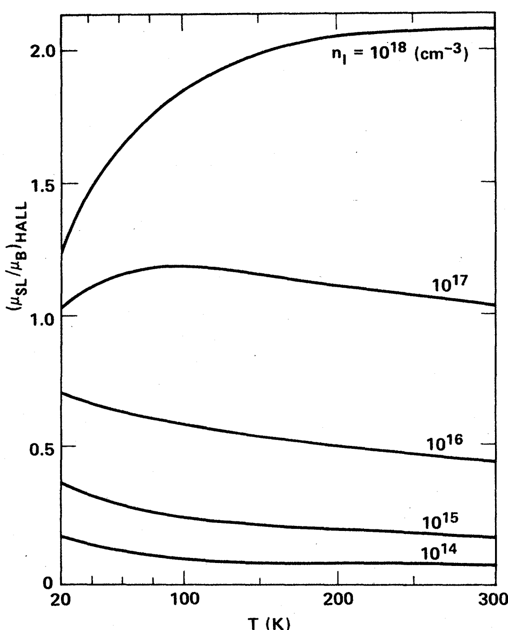

FIG. 14. Variation of the impurity-scattering-limited electron Hall mobility with temperature T for selected donor concentrations, as in Fig. 13.

A final noteworthy feature of the impurity-scattering-limited superlattice mobility not revealed in Figs. 11—14 is that it is predicted to increase linearly with layer thickness, as evidenced by the factor of s in Eq. (25). This is entirely a property of the cylindrical constant-energy surfaces and thus should also be present in the case of phonon scattering. Interestingly, the initial measurements[2] of room-temperature mobility in Si-$Si_{1-x}Ge_x$ superlattices did indeed show an increase with Si layer thickness, although apparently not with $Si_{1-x}Ge_x$ layer thickness.

IV. CONCLUSIONS

The tight-binding complex-band-structure method that we have developed has allowed us to make a comprehensive study of the electronic structure and impurity-scattering-limited mobility in prototype [100]-oriented silicon superlattices for arbitrarily thick layered systems. For layer thicknesses $l \geq 44$ Å, we predict that these structures will possess a direct energy-band gap at the center of the Brillouin zone (Γ point), established primarily by the zone folding of the bulk [100] and [$\bar{1}$00] conduction-band edges, and also that the band-edge transverse electron effective mass will saturate at 0.73 of the bulk conductivity effective mass. These trends appear to be relatively insensitive to the exact details of our model and apply to both Si-$Si_{1-x}Ge_x$ layered superlattices and hypothetical MOS and n-i-p-i superlattices.

Additional study will be required to determine if the direct nature of the superlattice band gap will significantly affect optical properties, as it does in many bulk semiconductors. For example, we have not attempted to address the question of whether or not electron-hole recombination rates will be enhanced in the superlattice. With regard to the possibility of a band-structure-driven enhancement of transverse electron mobility in silicon superlattices, on the other hand, the dominant controlling features of the electronic structure appear to be (i) the band-edge effective masses and (ii) the cylindrical nature of the constant-energy surfaces. Simple effective-mass scaling suggests a possible enhancement of 1.17 in the (low temperature) impurity-scattering limit and 2.20 in the (high temperature) electron-phonon scattering limit. Detailed consideration of the former case, however, demonstrates that the two-dimensional nature of the transport accompanying the cylindrical constant-energy surfaces introduces special dependences of the mobility on temperature, carrier concentration, and layer thickness. Nonetheless, for sufficiently high carrier concentrations we do find, in fact, that enhanced mobility is predicted. The quantitative results we have obtained for the impurity-scattering-limited mobility should be considered as upper limits to what could be expected in real systems. Neglected factors will undoubtedly tend to reduce the actual mobility, in particular interband scattering at higher carrier concentrations and alloy scattering in the case of a Si-$Si_{1-x}Ge_x$ superlattice. At the same time, these latter results take only partial advantage of the reduced-effective-mass enhancement mechanism, which should be much more effective in the case of phonon scattering.

ACKNOWLEDGMENTS

At the University of Cincinnati, this research was supported by U.S. National Aeronautics and Space Administration (NASA) Grant No. NAG-1-204. Part of this work was also performed under the auspices of the U.S. Department of Energy by Lawrence Livermore National Laboratory under Contract No. W-7405-Eng-48.

*Present address: SRI International, 333 Ravenswood Avenue, Menlo Park, CA 94025.

[1]J. A. Moriarty and S. Krishnamurthy, J. Appl. Phys. 54, 1892 (1983).

[2]H. M. Manasevit, I. S. Gergis, and A. B. Jones, Appl. Phys. Lett. 41, 464 (1982); J. Electron. Mater. 12, 637 (1983); A. B. Jones (private communication).

[3]J. C. Bean, L. C. Feldman, A. T. Fiory, S. Nakahara, and I. K. Robinson, J. Vac. Sci. Technol. A 2, 436 (1984); A. T. Fiory (private communication).

[4]R. People, J. C. Bean, D. V. Lang, A. M. Sergent, H. L. Störmer, K. W. Wecth, R. T. Lynch, and K. Baldwin, Appl. Phys. Lett. 45, 1231 (1984).

[5]F. Cerdeira, A. Pinczuk, and J. C. Bean, Phys. Rev. B 31, 1202 (1985), and references therein.

[6]G. C. Osbourn, Phys. Rev. B 27, 5126 (1983), and references

therein.
[7]P. J. Stiles, Surf. Sci. **73**, 252 (1978).
[8]For example, H. G. Craighead, Superlatt. Microstruct. (to be published).
[9]G. H. Döhler, Phys. Status Solidi B **52**, 79 (1972); **52**, 533 (1972).
[10]For example, G. H. Döhler, H. Künzel, D. Olego, K. Ploog, P. Ruden, H. J. Stolz, and G. Abstreiter, Phys. Rev. Lett. **47**, 846 (1981); P. Ruden and G. H. Döhler, Phys. Rev. B **27**, 3538 (1983); **27**, 3547 (1983).
[11]J. N. Schulman and Y. C. Chang, Phys. Rev. B **24**, 4445 (1981).
[12]W. A. Harrison, *Electronic Structure and the Properties of Solids* (Freeman, San Francisco, 1980).
[13]With a four-orbital-per-atom basis and two atoms per primative cell, the bulk Hamiltonian matrix is 8×8 in size, giving eight energy bands $E(\mathbf{k})$. Inverting each of these yields eight functions $\mathbf{k}(E)$, but since $-\mathbf{k}(E)$ is also a valid solution, one has 16 possible $\mathbf{k}$ states for each energy E.
[14]V. Heine, Proc. Phys. Soc. London **81**, 300 (1963).
[15]Y. C. Chang, Phys. Rev. B **25**, 605 (1982).
[16]R. Dingle, H. L. Störmer, A. C. Gossard, and W. Wiegmann, Appl. Phys. Lett. **33**, 665 (1978).
[17]S. Mori and T. Ando, J. Phys. Soc. Jpn. **48**, 865 (1980).
[18]S. M. Sze, *Physics of Semiconductor Devices* (Wiley, New York, 1969).
[19]R. A. Smith, *Semiconductors* (Cambridge University Press, New York, 1978).